

Terahertz optical Hall effect in monolayer MoS₂ in the presence of proximity-induced interactionsX. N. Zhao^{1,2}, W. Xu^{1,3,*}, Y. M. Xiao³, J. Liu³, B. Van Duppen⁴, and F. M. Peeters^{3,4}¹Key Laboratory of Materials Physics, Institute of Solid State Physics, Chinese Academy of Sciences, Hefei 230031, China²Chinese University of Science and Technology, Hefei 230026, China³School of Physics and Astronomy and Yunnan Key Laboratory for Quantum Information, Yunnan University, Kunming 650091, China⁴Department of Physics, University of Antwerp, Groenenborgerlaan 171, B-2020 Antwerpen, Belgium

(Received 25 March 2020; revised manuscript received 17 May 2020; accepted 19 May 2020; published 8 June 2020)

The effect of proximity-induced interactions such as Rashba spin-orbit coupling (SOC) and exchange interaction on the electronic and optical properties of n-type monolayer (ML) MoS₂ is investigated. We predict and demonstrate that the Rashba SOC can induce an in-plane spin splitting with terahertz (THz) energy, while the exchange interaction lifts the energy degeneracy in different valleys. Thus, spin polarization can be achieved in an n-type ML MoS₂ and valley Hall or optical Hall effect can be observed using linearly polarized THz radiation. In such a case, the transverse optical conductivity $\sigma_{xy}(\omega)$ results from spin-flip transition within spin-split conduction bands and from the fact that contributions from electrons with different spin orientations in different valleys can no longer be canceled out. Interestingly, we find that for fixed effective Zeeman field (or exchange interaction) the lowest spin-split conduction band in ML MoS₂ can be tuned from one in the K valley to another one in the K' valley by varying the Rashba parameter λ_R . Therefore, by changing λ_R we can turn the sign of the spin polarization and $\text{Im}\sigma_{xy}(\omega)$ from positive to negative. Moreover, we find that the dominant contribution of the selection rules to $\sigma_{xx}(\omega)$ is from electrons in the K valley and to $\sigma_{xy}(\omega)$ is from electrons in the K' valley. These important and interesting theoretical findings can be helpful to experimental observation of the optical Hall effect in valleytronic systems using linearly polarized THz radiation fields.

DOI: [10.1103/PhysRevB.101.245412](https://doi.org/10.1103/PhysRevB.101.245412)**I. INTRODUCTION**

In recent years, the investigation of transition metal dichalcogenide (TMD) based two-dimensional (2D) electronic systems has been a hot and fast-growing field of research in condensed matter physics, electronics and optics owing to their unique valleytronic properties [1,2] for potential applications in, e.g., information technology [3–5]. The discovery of the 2D TMD based valleytronic systems has also led to the proposal and observation of novel transport effects such as valley Hall effect (VHE) [1,6,7] which is electrically equivalent to the Hall effect observed in the presence of a perpendicular magnetic field. One of the most interesting features of a free-standing valleytronic material is that the electron energies are degenerate around K and K' points [8–10], but the electronic spin orientations around these two valleys are just opposite [11]. Thus, the electronic band structure exhibits the Berry curvature [1,12] and the electrons with different spin orientations can move along different directions under the action of driving electric and/or electromagnetic (EM) field [13,14]. Therefore, the experimental setup for the measurement of the VHE is similar to that used to detect the spin Hall effect [15]. The VHE in monolayer (ML) TMD such as ML MoS₂ was first observed experimentally in 2014 by measuring the Hall voltage under the action of a circularly polarized EM field in the visible band, where the radiation field plays the

role of creating an imbalance between the two valleys [16]. The VHE was also directly imaged in ML MoS₂ transistors via magneto-optical Kerr rotation microscopy [17,18] where a circularly polarized radiation field in the visible to infrared bandwidth was applied.

It should be noted that at present, the VHE in 2D TMDs has been mainly observed by using circularly polarized EM field in the infrared and the visible [19,20]. In such a case, the pumping EM field can selectively excite electrons in different valleys with different spin orientations via interband electronic transitions accompanied by the absorption of photons. It is known that the Hall effect is basically a consequence of the nonzero transverse conductivity. Therefore, it is desirable to be able to observe the VHE in 2D TMDs using linearly polarized light radiation. The problem now is that the electron energies degenerate around the K and the K' points in a time-inversion symmetric 2D TMD system. Under the action of a linearly polarized radiation field, the current densities for electrons moving from two valleys are equal in magnitude but with opposite directions. As a result, the overall transverse voltage is canceled out and, thus, the VHE cannot be observed under linearly polarized light radiation in a free-standing 2D TMD system. A way out of this is by breaking the valley degeneracy. One of the most efficient schemes to lift valley degeneracy in a 2D TMD material is to place the TMD film on a dielectric or ferromagnetic substrate [21,22]. In such a case, the proximity effect induced by the presence of the substrate can result in a Rashba spin-orbit coupling (SOC) [23–25] and/or an exchange interaction [26]. The

*wenxu_issp@aliyun.com

Rashba SOC can induce a spin splitting and an in-plane electronic spin. Previous theoretical results [27] have indicated that the splitting of the conduction and valence band via Rashba SOC can be, respectively, in the terahertz (THz) and in the far-to-mid infrared bandwidth for ML MoS₂. Moreover, proximity-induced exchange interaction can lift the valley degeneracy of the electronic energy spectrum due to the introduction of a magnetic momentum [21] and/or van der Waals force in a 2D TMD system [26]. Hence, in the presence of particular substrates the proximity-induced interactions can be utilized for the observation of the VHE in 2D TMD systems using linearly polarized EM radiation. Because the spin splitting of the conduction band in ML MoS₂ is in THz frequency regime [27]. One would expect that the VHE or the optical Hall effect can be observed by using advanced THz techniques such as THz time-domain spectroscopy (THz TDS) [28–30] in which the THz radiation source is highly linearly polarized. Recently, we studied theoretically the effects of the Rashba SOC on the THz optoelectronic properties of ML MoS₂ [27] in the absence of exchange interaction. We found that in the presence of a linearly polarized THz field, spin-flip transitions can be achieved in n-type ML MoS₂ and a nonzero transverse optical conductivity $\sigma_{xy}(\omega)$ can be observed in different valleys. It was shown that in the absence of the proximity-induced exchange interaction, the imaginary part of $\sigma_{xy}(\omega)$ in different valleys has the same value but with different signs, so that the overall contributions to $\sigma_{xy}(\omega)$ from two valleys are canceled out.

In this study, we re-examine the problem by including proximity-induced exchange interaction. We take ML MoS₂ as an example and evaluate the dependence of the longitudinal and transverse optical conductivities on the strength of the Rashba SOC and the proximity-induced exchange interaction. To realize electronic and optoelectronic devices, the ML MoS₂ is often placed on a substrate, similar as for conventional semiconductor based devices. Very recently, we experimentally measured the optical properties of ML MoS₂ on different substrates using THz TDS technique [31]. We found that n-type ML MoS₂ has a strong response to the linearly polarized THz field. One of our major motivations of this study is to explore the possibility to observe the optical Hall effect in n-type ML MoS₂ by using, e.g., THz TDS measurement. The paper is organized as follows. The theoretical approaches developed in this study are presented in Sec. II, where we study the electronic band structure, the in-plane spin orientation, the spin polarization, and the optical conductivity under linearly polarized THz radiation field. The obtained results are presented and discussed in Sec. III and the concluding remarks are summarized in Sec. IV.

II. THEORETICAL APPROACH

A. Electronic band structure

When ML MoS₂ is placed on a substrate, proximity-induced interactions can take place. Generally, the Hamiltonian to describe a low-energy electron in a 2D TMD system placed on a substrate can be composed of four basic parts [21]

$$H = H_0 + H_{\text{SOC}} + H_R + H_{\text{ex}}, \quad (1)$$

with

$$\hat{H}_0 = \left[A(\zeta k_x \hat{\sigma}_x + k_y \hat{\sigma}_y) + \frac{\Delta}{2} \hat{\sigma}_z \right] \otimes \hat{\sigma}_0, \quad (1a)$$

$$\hat{H}_{\text{SOC}} = \zeta [\lambda_c \hat{\sigma}_+ + \lambda_v \hat{\sigma}_-] \otimes \hat{s}_z, \quad (1b)$$

$$\hat{H}_R = \lambda_R [\zeta \hat{\sigma}_x \otimes \hat{s}_y - \hat{\sigma}_y \otimes \hat{s}_x], \quad (1c)$$

and

$$\hat{H}_{\text{ex}} = -[B_c \hat{\sigma}_+ + B_v \hat{\sigma}_-] \otimes \hat{s}_z, \quad (1d)$$

being, respectively, the contribution from orbital interaction, intrinsic spin-orbit coupling (SOC), Rashba SOC, and from proximity-induced exchange. Here, $\mathbf{k} = (k_x, k_y)$ is the electron wave vector or momentum operator along the 2D plane, $\zeta = \pm$ refers to the K (K') valley, $A = at$ with a being the lattice parameter and t the hopping parameter [1], the intrinsic SOC parameters $2\lambda_c$ and $2\lambda_v$ are the energies for intrinsic spin splitting, respectively, in the conduction and valence bands in the absence of proximity-induced interactions [1,32], B_c and B_v are effective Zeeman fields experienced, respectively, by an electron in the conduction and valence bands in the presence of exchange coupling with the substrate, Δ is the direct band gap between the valence and conduction bands [1,33,34], and $\lambda_R = \alpha_R \Delta / (2at)$ is induced by Rashba SOC with α_R being the Rashba parameter [35,36]. Furthermore, the Pauli matrices \hat{s}_α and $\hat{\sigma}_\alpha$ refer, respectively, to real spin and to orbital pseudospin with $\alpha = (x, y, z)$, $\hat{\sigma}_0$ is a unit 2×2 matrix, and $\hat{\sigma}_\pm = (\hat{\sigma}_0 \pm \hat{\sigma}_z)/2$. It should be noted that the *pseudospin* used here is a simple Pauli mathematical concept to mark different electronic states in a two-state quantum system, which can be applied to describe the orbital degree of freedom in order to distinguish from the real spin [21]. Moreover, in the Hamiltonian given by Eq. (1), the wave functions $|\phi_\beta^\zeta, s\rangle$ are taken as the basis, with $\beta = (c, v)$ referring to the conduction and valence band and $s = \pm$ to the spin-split state. For ML MoS₂, $|\phi_c^\zeta, s\rangle = |d_z^2\rangle$ and $|\phi_v^\zeta, s\rangle = (|d_{x^2+y^2}\rangle + i\zeta |d_{xy}\rangle)/\sqrt{2}$ are, respectively, the wave functions of conduction band minima and valence band maxima, which are composed of different d orbits of Mo.

The H_0 and H_{SOC} terms are always present in a 2D TMD, while H_{ex} and H_R terms are mainly induced by the proximity effect in the presence of a substrate. We know that ML MoS₂ is a 2D hexagonal crystal with uniaxial symmetry. In such a crystal system, Rashba SOC often exists [37,38]. When ML MoS₂ is placed on a substrate, the presence of the heterostructure can lead to an inversion symmetry breaking field along the direction normal to the 2D plane of ML MoS₂ [21,22]. This may further enhance the Rashba SOC [24,39,40]. Furthermore, the presence of the dielectric and/or magnetic substrate can result in an exchange interaction in ML MoS₂, due to the introduction of the effective Zeeman field by van der Waals force in the film/substrate heterostructure [26], which introduces the H_{ex} term in Eq. (1).

Eq. (1) can be written as a 4×4 matrix

$$\hat{H} = \begin{bmatrix} \Delta/2 + d_\zeta^c & 0 & Ak_\zeta^- & 0 \\ 0 & \Delta/2 - d_\zeta^c & i2\lambda_R & Ak_\zeta^- \\ Ak_\zeta^+ & -i2\lambda_R & -\Delta/2 + d_\zeta^v & 0 \\ 0 & Ak_\zeta^+ & 0 & -\Delta/2 - d_\zeta^v \end{bmatrix} \quad (2)$$

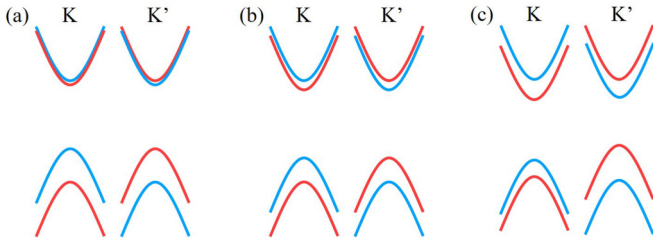


FIG. 1. Schematic band structure at two valleys of ML MoS₂. Here, (a) is the case with only H_0 and H_{SOC} terms, (b) is with H_0 , H_{SOC} , and H_R terms, and (c) is with H_0 , H_{SOC} , H_R , and H_{ex} terms. The electronic states with up/down spins are presented by blue/red curves.

with $k_\zeta^\pm = \zeta k_x \pm ik_y$, $d_\zeta^\beta = \lambda_\beta - \zeta B_\beta$, and $\beta = (c, v)$. The corresponding Schrödinger equation for an electron in the valley K (K') can be solved analytically. The four eigenvalues are the solutions of the equation

$$E^4 - A_2 E^2 + A_1 E + A_0 = 0, \quad (3)$$

with

$$A_2 = \frac{\Delta^2}{2} + 4\lambda_R^2 + 2A^2 k^2 + d_\zeta^{v2} + d_\zeta^{c2}, \quad (3a)$$

$$A_1 = \Delta(d_\zeta^{v2} - d_\zeta^{c2}) - 4\lambda_R^2(d_\zeta^v - d_\zeta^c), \quad (3b)$$

and

$$A_0 = \left(\frac{\Delta^2}{4} + A^2 k^2 \right)^2 + \lambda_R^2 (\Delta + 2d_\zeta^c) (\Delta + 2d_\zeta^d) - \frac{\Delta^2}{4} (d_\zeta^{c2} + d_\zeta^{v2}) - 2A^2 k^2 d_\zeta^c d_\zeta^v + (d_\zeta^c d_\zeta^v)^2. \quad (3c)$$

The results shown in Eq. (2) and Eq. (3) reflect the basic roles played by different interaction terms in Eq. (1) in affecting the electronic band structure. In Fig. 1 we plot the schematic band structures with different interactions to show more clearly the effect of each term in Hamiltonian in Eq. (1). (i) The orbital interaction H_0 results in the energy dispersion of the conduction and valence bands in K and K' valleys. In the absence of other interaction terms, the energy spectra in K and K' valleys are degenerate. (ii) The intrinsic SOC, H_{SOC} , and the proximity-induced exchange, H_{ex} , contribute only to the diagonal elements of the Hamiltonian matrix in Eq. (2). They affect the actual energy positions of the conduction and valence bands. (iii) In the absence of Rashba SOC (i.e., $H_R = 0$), when $H_{\text{ex}} \neq 0$ and $H_{\text{SOC}} \neq 0$ Eq. (2) can be reduced into a 2×2 matrix

$$H(\mathbf{k}) = \begin{bmatrix} \Delta/2 + sd_\zeta^c & Ak_\zeta^- \\ Ak_\zeta^+ & -\Delta/2 + sd_\zeta^v \end{bmatrix}, \quad (4)$$

with $s = \pm$ referring to the splitting in the conduction and valence bands. When $H_R = H_{\text{ex}} = 0$, Eq. (4) becomes the commonly used equation for simplified calculations [41]. In such a case, the electronic energies in K and K' valleys are degenerate and the splitting of the conduction band is weak [see Fig. 1(a)]. (iv) The Rashba SOC, H_R , cannot break the time reversal symmetry. However, it introduces an in-plane spin and leads to an extra term in Eq. (2) that modulates the

band splitting, while it keeps energy symmetry for the two valleys as shown in Fig. 1(b). (v) In the presence of H_{ex} term, the splitting in the conduction and valence bands depends on the valley index. Thus, the valley degeneracy of the electronic energy spectra is lifted [see Fig. 1(c)]. As a result, when a ML MoS₂ is placed on a substrate, the substrate induced effects such as the Rashba SOC (i.e., the H_R term) and the exchange interaction (i.e., the H_{ex} term) can lift the energy degeneracy in K and K' valleys.

The corresponding eigenfunctions for electronic states near the K and K' points are

$$|\mathbf{k}; \lambda\rangle = \mathcal{A}[c_1, c_2, c_3, c_4]e^{i\mathbf{k}\cdot\mathbf{r}}, \quad (5)$$

where $\lambda = (\beta, \zeta, s)$ with $\beta = (c, v)$ referring to conduction or valence band and $s = \pm$ to spin-split band,

$$c_1 = -2i\lambda_R A^2 k_\zeta^{-2}, \quad (5a)$$

$$c_2 = Ak_\zeta^- h_1, \quad (5b)$$

$$c_3 = -2i\lambda_R Ak_\zeta^- h_0, \quad (5c)$$

$$c_4 = h_2, \quad (5d)$$

and

$$\mathcal{A} = (|c_1|^2 + |c_2|^2 + |c_3|^2 + |c_4|^2)^{-\frac{1}{2}} \quad (5e)$$

is the normalization coefficient. Here, $h_0 = E - \Delta/2 - d_\zeta^c$, $h_1 = (E - \Delta/2 - d_\zeta^c)(E + \Delta/2 - d_\zeta^v) - A^2 k^2$, and $h_2 = (E - \Delta/2 + d_\zeta^c)h_1 - 4\lambda_R^2 h_0$.

B. In-plane spin orientation and polarization

To observe and understand the optical Hall effect in the THz regime induced by intraband electronic transitions, it is necessary to examine the in-plane spin orientation in spin-split states in different valleys and bands with the quantum number $\lambda = (\beta, \zeta, s)$. With the electron wave function obtained for a 2D TMD, the strength of the in-plane spin orientation along the x and y directions can be calculated by using the spin operator

$$O_\alpha = \langle \tau, \mathbf{k} | \sigma_0 \otimes s_\alpha | \mathbf{k}, \tau \rangle. \quad (6)$$

By doing so, we have

$$O_x(\mathbf{k}) = \frac{c_1 c_2^* + c_2 c_1^* + c_3 c_4^* + c_4 c_3^*}{A^2} = -P_\zeta(k) \sin\theta, \quad (6a)$$

and

$$O_y(\mathbf{k}) = i \frac{c_1 c_2^* - c_2 c_1^* + c_3 c_4^* - c_4 c_3^*}{A^2} = \zeta P_\zeta(k) \cos\theta, \quad (6b)$$

with θ being the angle between \mathbf{k} and the x axis, $P_\zeta(k) = \lambda_R G_\zeta A k / A^2$ and $G_\zeta = 4(A^2 k^2 h_0 + h_1 h_2)$. Equation (6) indicates that the in-plane spin of electrons in a 2D TMD is induced by the Rashba SOC and it vanishes when $\lambda_R = 0$. Apparently we have $[O_x(\mathbf{k})]^2 + [O_y(\mathbf{k})]^2 = |P_\zeta(k)|^2$ and, thus, the projection of the in-plane spin orientation in the \mathbf{k} plane is a circle with $|P_\zeta(k)|$ being the radius. Namely, $|P_\zeta(k)|$ can be taken as the magnitude of the in-plane spin orientation. We note that the terms h_0 , h_1 , and h_2 in $G_\zeta(k)$ depend on the valley index ζ . This implies that in the presence of the Rashba SOC and the exchange interaction, the amplitude of

the in-plane spin orientation for each spin-split conduction or valence bands in different valleys is generally different.

Because the degeneracy of the electron energies in different valleys can be lifted and the in-plane spin orientation in different valleys are different due to the proximity-induced interactions, the 2D TMD based electronic system can be spin polarized. In the present study, we focus on n-type ML MoS₂ with electron density n_e . When ML MoS₂ is subjected to THz irradiation, the effect of photon-generated carriers can be neglected because the photon energy of THz EM field (1 THz \simeq 4.13 meV) is much smaller than the forbidden gap (about 1.66 eV) between the conduction and valence bands of ML MoS₂. Applying the condition of electron number conservation, the Fermi energy (or chemical potential) for electrons in the conduction band is determined by

$$n_e = \sum_{\mathbf{k}, \zeta, s} f(E_s^\zeta(\mathbf{k})) = n_+^+ + n_+^- + n_-^+ + n_-^-, \quad (7)$$

where $f(x) = [1 + \exp((x - E_F)/k_B T)]^{-1}$ is the Fermi-Dirac function with E_F being the Fermi energy or chemical potential, $E_s^\zeta(\mathbf{k})$ is the electron energy in conduction band, and $n_s^\zeta = \sum_{\mathbf{k}} f(E_s^\zeta(\mathbf{k}))$ is the electron density in a spin-split band s in valley ζ . Thus, the in-plane spin polarization is given by

$$S = \frac{(n_+^+ + n_+^-) - (n_-^+ + n_-^-)}{n_e}. \quad (8)$$

When $S \neq 0$, the electronic system is spin polarized.

C. Optical conductivity

In this study, we consider an n-type ML MoS₂ subjected to a relatively weak THz radiation field which is polarized linearly along the 2D plane of the ML MoS₂. We employ the Kubo-Greenwood formula to evaluate the longitudinal and transverse optical conductivities. In the optical or long-wavelength limit and within the linear response approximation, the Kubo-Greenwood formula for a 2D electronic system takes the form [42]

$$\sigma_{\alpha\alpha'}(\omega) = \frac{ie^2 n_e}{m^* \tilde{\omega}} \delta_{\alpha\alpha'} + \frac{ie^2}{\omega} \sum_{\mathbf{k}', \mathbf{k}; \lambda', \lambda} W_{\lambda'\lambda}^{\alpha\alpha'}(\mathbf{k}', \mathbf{k}) \Pi_{\lambda'\lambda}(\mathbf{k}', \mathbf{k}; \tilde{\omega}), \quad (9)$$

where $(\alpha, \alpha') = (x, y)$ for a 2D system, n_e is the electron density in the system, m^* is the effective electron mass, $\tilde{\omega} = \omega + i\eta$ with ω being the photon frequency and $\eta \rightarrow 0^+$, $v_\alpha = \hbar^{-1} \partial \hat{H} / \partial k_\alpha$ is the group velocity for an electron, the interaction matrix element is given by

$$W_{\lambda'\lambda}^{\alpha\alpha'}(\mathbf{k}', \mathbf{k}) = \langle \lambda, \mathbf{k} | v_\alpha | \mathbf{k}', \lambda' \rangle \langle \lambda', \mathbf{k}' | v_{\alpha'} | \mathbf{k}, \lambda \rangle, \quad (9a)$$

and

$$\Pi_{\lambda'\lambda}(\mathbf{k}', \mathbf{k}; \tilde{\omega}) = \frac{f[E_\lambda(\mathbf{k})] - f[E_{\lambda'}(\mathbf{k}')] }{E_\lambda(\mathbf{k}) - E_{\lambda'}(\mathbf{k}') + \hbar \tilde{\omega}}, \quad (9b)$$

is the pair bubble or electronic density-density correlation function. This formula implies that for intraband electronic transitions (i.e., $\lambda' = \lambda$), the contribution from the second term in Eq. (9) is zero so that the transverse optical conductivity $\sigma_{xy}(\omega) = \sigma_{yx}(\omega) = 0$. In such a case, the longitudinal conductivity becomes the well-known Drude formula:

$\sigma_{xx}(\omega) = \sigma_{yy}(\omega) = \sigma_0 / (1 - i\omega\tau)$, where $\sigma_0 = e^2 n_e \tau / m^*$ is the dc conductivity when taking $\eta \rightarrow \tau^{-1}$ with τ being the transport relaxation time for electrons. Using the electron wave function for a ML TMD, we obtain for the velocity matrix elements

$$\langle \lambda', \mathbf{k}' | v_x | \mathbf{k}, \lambda \rangle = \frac{\zeta A}{\hbar \mathcal{A} \mathcal{A}'} (c_1'^* c_3 + c_2'^* c_4 + c_3'^* c_1 + c_4'^* c_2)$$

and

$$\langle \lambda', \mathbf{k}' | v_y | \mathbf{k}, \lambda \rangle = \frac{iA}{\hbar \mathcal{A} \mathcal{A}'} (-c_1'^* c_3 - c_2'^* c_4 + c_3'^* c_1 + c_4'^* c_2).$$

Thus, we obtain the selection rules

$$W_{\lambda'\lambda}^{xx}(\mathbf{k}', \mathbf{k}) = \frac{A^4 k^2 p^2 + q^2 + 2pq \cos(2\theta)}{\hbar^2 \mathcal{A}^2 \mathcal{A}'^2} \delta_{\mathbf{k}, \mathbf{k}'}, \quad (9c)$$

and

$$W_{\lambda'\lambda}^{xy}(\mathbf{k}', \mathbf{k}) = \frac{\zeta A^4 k^2 i(p^2 - q^2) + 2\zeta pq \sin(2\theta)}{\hbar^2 \mathcal{A}^2 \mathcal{A}'^2} \delta_{\mathbf{k}, \mathbf{k}'}, \quad (9d)$$

where $p = 4\lambda_R^2 A^2 k^2 h'_0 + h_1 h'_2$ and $q = 4\lambda_R^2 A^2 k^2 h_0 + h'_1 h_2$. Due to the symmetry of the electronic energy spectrum, we get $\sigma_{xx}(\omega) = \sigma_{yy}(\omega)$ and $\sigma_{xy}(\omega) = \sigma_{yx}(\omega)$.

It should be noted that the inter-valley electronic transitions require large electron momentum transfer in a ML MoS₂. This mechanism is almost impossible for direct electron-photon interaction which does not alter the electron momentum, as expressed by the $\delta_{\mathbf{k}, \mathbf{k}'}$ term in Eqs. (9c) and (9d). Hence, the total or overall optical conductivity of the ML MoS₂ system can be regarded as the sum over the contributions from the two valleys, that is

$$\sigma_{\alpha\alpha'}(\omega) = \sum_{\zeta=\pm} \sigma_{\alpha\alpha'}^\zeta(\omega), \quad (10)$$

where $\sigma_{\alpha\alpha'}^\zeta(\omega)$ can be calculated for each valley. For the case where only the conduction band is taken into account and only the process of optical absorption is considered, the longitudinal and transverse (or Hall) optical conductivities at valley ζ are obtained, respectively, as

$$\sigma_{xx}^\zeta(\omega) = \sigma_D(\omega) + \sigma_{xx,s}^\zeta(\omega), \quad (11)$$

$$\sigma_{xx,s}^\zeta(\omega) = \int_0^\infty dk \frac{ie^2 A^4 k^3 p^2 + q^2}{2\pi \hbar^3 \omega \mathcal{A}^2 \mathcal{A}'^2} \Pi_{ss'}^\zeta(k) \delta_{\mathbf{k}, \mathbf{k}'}, \quad (11a)$$

and

$$\sigma_{xy}^\zeta(\omega) = \zeta \int_0^\infty dk \frac{-e^2 A^4 k^3 p^2 - q^2}{2\pi \hbar^3 \omega \mathcal{A}^2 \mathcal{A}'^2} \Pi_{ss'}^\zeta(k) \delta_{\mathbf{k}, \mathbf{k}'}, \quad (12)$$

where $\sigma_D(\omega) = (e^2 n_e \tau / m^*) (1 + i\omega\tau)^{-1}$ is the Drude optical conductivity caused by intra-subband electronic transition. The conductivity $\sigma_{xx,s}^\zeta(\omega)$ is induced by spin-flip transition in split conduction band, and

$$\Pi_{ss'}^\zeta(k) = \frac{f[E_s^\zeta(k)] - f[E_{s'}^\zeta(k)]}{\omega + \omega_{ss'}^\zeta(k) + i/\tau_s^e},$$

with $E_s^\zeta(k)$ being the spin-split electron energy in the conduction band in valley ζ and $\omega_{ss'}^\zeta(k) = [E_s^\zeta(k) - E_{s'}^\zeta(k)]/\hbar$ being the change in electron energy from the initial to the final states accompanied by the absorption of a photon. In this study we use a spin relaxation time τ_s^e for spin-flip transitions in the

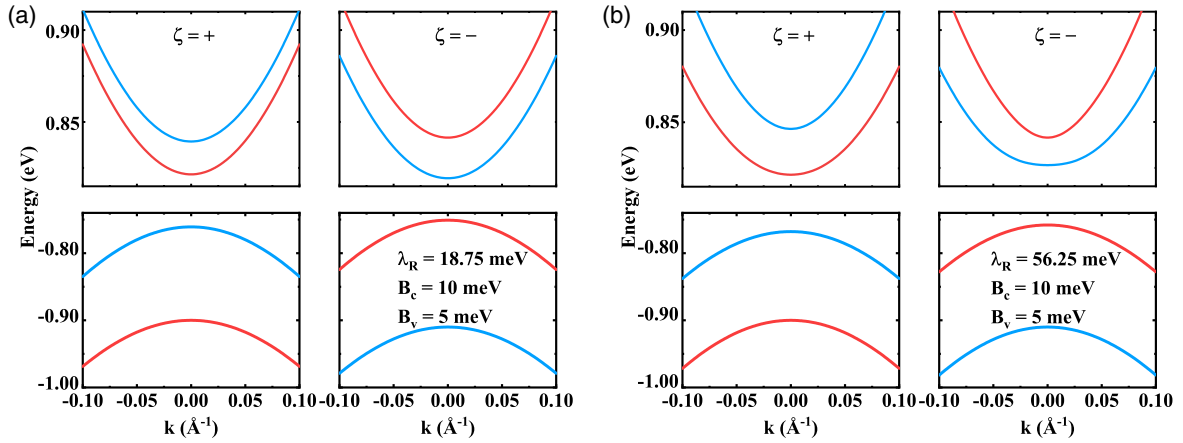


FIG. 2. The conduction (upper panels) and valence (lower panels) band structure at the two valleys ($\zeta = \pm$) in ML MoS₂. The spin up/down states are represented by blue/red curves and the results are obtained by taking $B_c = 10$ meV and $B_v = 5$ meV for a small Rashba parameter $\lambda_R = 18.75$ meV in (a) and a relatively larger $\lambda_R = 56.25$ meV in (b).

split conduction bands [43,44]. Moreover, it should be noticed that $\sigma_{\alpha\alpha'}^{\zeta}(\omega)$ has real and imaginary parts. It is known [45] that the real part of the optical conductivity corresponds to dissipation or optical absorption, whereas the imaginary part describes the energy exchange processes between electrons and the radiation field, which does not change the energy of the electron-field system.

III. RESULTS AND DISCUSSIONS

In this study, we consider a n-type ML MoS₂ placed on a substrate. The material and theoretical parameters used in the numerical calculation are [1,32–34]: $a = 3.193$ Å, $t = 1.1$ eV, $A = at = 3.5123$ Å eV, $\Delta = 1.66$ eV, $2\lambda_c = 3$ meV, and $2\lambda_v = 150$ meV. The calculations are carried out by considering only the spin-split conduction bands in different valleys. When calculating the optical conductivity from Eqs. (11) and (12), we take the spin relaxation time for inter-subband or spin-flip transitions as $\tau_s^e = 3$ ps [46]. Because the values of the Rashba parameter λ_R and the effective Zeeman field B_c and B_v can be tuned experimentally, we take them as variable input parameters in our calculations. Additionally, we note that the values of B_c and B_v are usually different since they reflect different effective Landé g factors for Bloch states [21].

A. Electronic band structure

In Fig. 2(a) we show the low-energy electronic band structure with spin-split ($s = \pm$) conduction and valence bands in the different valleys ($\zeta = \pm$) for fixed Rashba parameter $\lambda_R = 0.25\lambda_v = 18.75$ meV and effective Zeeman field factors $B_c = 10$ meV and $B_v = 5$ meV. We notice the following features. (i) The spin splitting in the conduction (upper panels) and valence (lower panels) bands are enhanced due to proximity-induced interactions. An observable spin splitting in THz range can be seen in the conduction band in spite of taking a very small value for the intrinsic SOC parameter λ_c , (ii) the energy spectra for electrons in the different valleys are different and the energy degeneracy for spin-split conduction and valence bands in different valleys is lifted due to the presence of the proximity-induced interactions, and (iii) the electrons in

the different spin-split bands and valleys have different spin states (presented by blue and red curves). For comparison, in Fig. 2(b) we present the electronic band structure for a larger Rashba parameter $\lambda_R = 0.75\lambda_v = 56.25$ meV with the same values of B_c and B_v . More interesting phenomena can be found as follows. The spin splitting in the conduction band in K valley ($\zeta = +$) becomes larger than that in K' valley ($\zeta = -$), which is just opposite to the previous case for small Rashba parameter (left panel). From Eq. (2) we know that the exchange interaction, B_c and B_v , has opposite effects on the energy spectra in the different valleys, while the Rashba SOC can lead to energy splitting for both valleys. So in this case the relative small exchange interaction cannot cancel out the strong effect of the large Rashba effect on the spin splitting in the K' valley ($\zeta = -$). The effect of spin splitting on the valence band does not change significantly because the intrinsic spin splitting in the valence band is large and the combined effect of the Rashba SOC and the exchange interaction does not make a big difference between the two valleys. Moreover, the spin orientation in each split band remains unchanged.

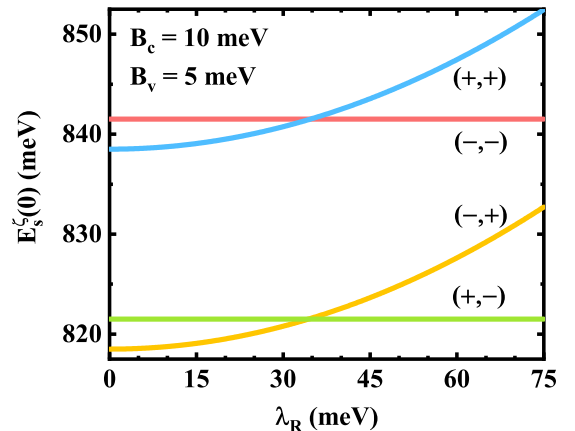


FIG. 3. The minima of four conduction subbands ($\zeta = \pm, s = \pm$) as a function of Rashba parameter λ_R for fixed values of $B_c = 10$ meV and $B_v = 5$ meV.

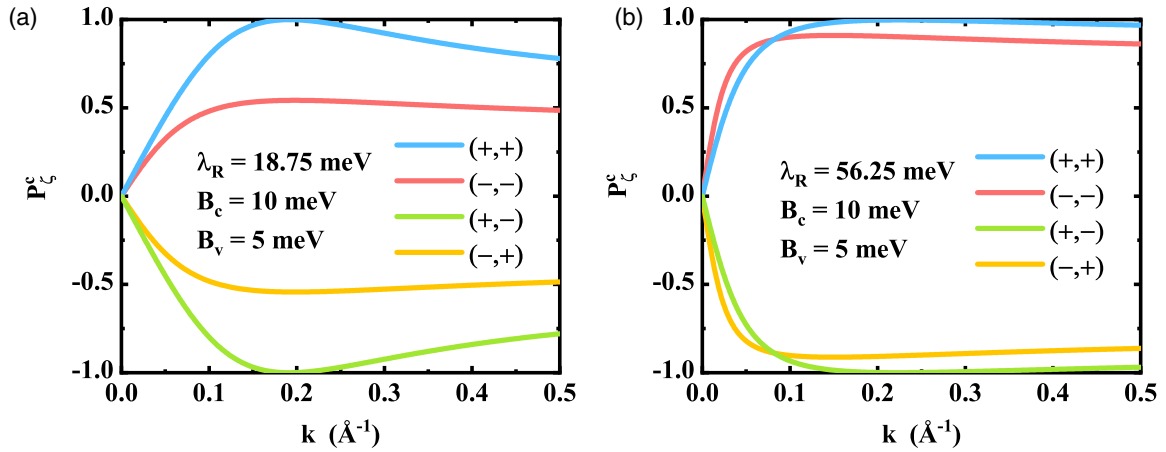


FIG. 4. The size of in-plane spin orientation [$P_\zeta(k)$ in Eq. (6)] as a function of electron wave vector at fixed effective Zeeman fields $B_c = 10$ meV and $B_v = 5$ meV for Rashba parameter $\lambda_R = 18.75$ meV (left panel) and $\lambda_R = 56.25$ meV (right panel) in the spin-split conduction bands. Here (ζ, s) stands for spin-split subband with $\zeta = \pm$ and $s = \pm$ being the valley and the spin index, respectively.

In Fig. 3 we plot the minima of four split conduction bands, $E_s^\zeta(0)$ with valley and spin indexes (ζ, s) , as a function of Rashba parameter λ_R for the fixed effective Zeeman field factors $B_c = 10$ meV and $B_v = 5$ meV. We find that: (i) the bottoms of the spin-up conduction bands in the two valleys $(\zeta, +)$ increase in energy with increasing λ_R , while those of the spin-down bands $(\zeta, -)$ depend very weakly on λ_R , (ii) the exchange interaction leads to different energy gaps between the split conduction bands in different valleys, so that the spin splitting of the conduction bands in K valley ($\zeta = +$) increases and that in K' valley ($\zeta = -$) decreases with increasing λ_R , and (iii) the lowest conduction band is $(\zeta, s) = (-, +)$ at small values of λ_R and becomes $(\zeta, s) = (+, -)$ for large values of λ_R , where the turning point is around $\lambda_R = 34.5$ meV at which the Rashba effect and the exchange interaction cancel each out so that the minima of the conduction bands $E_+^-(0) \simeq E_+^+(0)$. Hence, the most interesting result shown in Fig. 3 is that by varying the Rashba parameter we can tune the minimum of the conduction band in ML MoS₂ from spin-up states in K' valley to spin-down states in K valley.

B. Spin orientation and polarization

From Eq. (1d) we see that the Rashba term H_R in the electron Hamiltonian can lead to electron spin component in the xy plane and a hybridization of the conduction and valence bands. As a result, the electronic spin in ML MoS₂ now has an in-plane component and consequently the spin is no longer a good quantum number [21,47]. It should be noted that although now s is no longer a good quantum number, we take commonly used $s = \pm$ or up/down for the sake of distinguishing different electronic states induced by spin splitting. Because the electronic spin plays an important role in the observation of the optical Hall effect, here we discuss the features of the electronic spin in the split conduction bands in ML MoS₂.

From Eq. (6) we note that the strength and sign of the in-plane spin orientation for each spin-split band in ML MoS₂

is determined by $P_\zeta(k)$, from which we obtain the strength and sign of $O_x(\mathbf{k})$ and $O_y(\mathbf{k})$ along with the direction of the in-plane spin orientation for the spin-split bands in different valleys. In Fig. 4, we plot $P_\zeta(k)$ vs k with $B_c = 10$ meV and $B_v = 5$ meV for split conduction bands with index (ζ, s) at $\lambda_R = 18.75$ meV in the left panel and at $\lambda_R = 56.25$ meV in the right panel. We find that: (i) $P_\zeta(k)$ does not change sign with varying electron wave vector in each band; (ii) the strongest effect of the in-plane spin orientation occurs at nonzero k ; (iii) the relative strength of the in-plane spin orientation for the different valleys depends on the band gap between the conduction and valence bands in a valley, where the valley with a smaller band gap has the larger in-plane spin orientation; (iv) the crossover of the curves in Fig. 4(b) is caused by the change of the band gap in different valleys with increasing k at $\lambda_R = 56.25$ meV; (v) $P_\zeta(k)$ does not change sign with varying λ_R ; (vi) the sign of $P_\zeta(k)$ for spin-up band is opposite to that for spin-down band in a given valley; (vii) $P_\zeta(k)$ has the same sign for higher $[(+, +), (-, -)]$ or lower

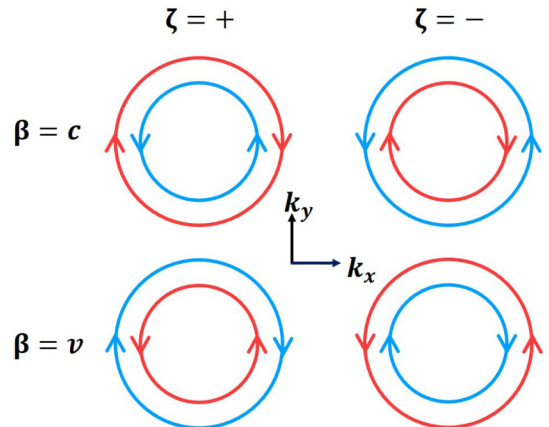


FIG. 5. Schematic presentation of the in-plane spin orientation in spin-split ($s = \pm$) conduction ($\beta = c$) and valence ($\beta = v$) bands in K ($\zeta = +$) and K' ($\zeta = -$) valleys.

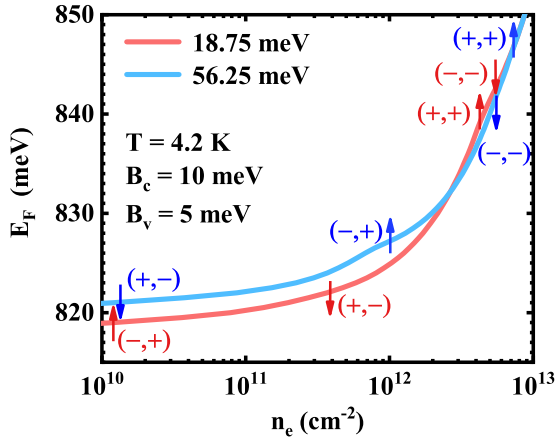


FIG. 6. Fermi energy as a function of total electron density n_e at $T = 4.2$ K for $\lambda_R = 18.75$ meV (red curve) and $\lambda_R = 56.25$ meV (blue curve) for fixed $B_c = 10$ meV and $B_v = 5$ meV. The red and blue arrows indicate the lowest energy $E_s^\zeta(0)$ of the four spin-split conduction subbands with $(\zeta = \pm, s = \pm)$.

$[(+, -), (-, +)]$ bands. Similar results can be found for the spin-split valence bands. Furthermore, we find that $O_y(\mathbf{k})$ for spin-up has the opposite sign as $O_x(\mathbf{k})$ for spin-up in K valley and has the same sign to $O_x(\mathbf{k})$ for spin-down in K' valley. $O_x(\mathbf{k})$ and $O_y(\mathbf{k})$ change sign for different spin-split bands in conduction or valence band in a certain valley. Thus, in ML MoS₂ the sign of the in-plane spin orientation is opposite in two valleys ($\zeta = \pm$) and in the spin-split bands ($\beta = c/v, s = \pm$) no matter the values of λ_R, B_c and B_v as long as $\lambda_R \neq 0$. From the fact that the direction of the in-plane spin orientation is parallel to the corresponding electron wave vector \mathbf{k} , we present in Fig. 5 schematically the in-plane spin orientation in spin-split bands ($s = \pm$) in the conduction ($\beta = c$) and valance ($\beta = v$) bands in K ($\zeta = +$) and K' ($\zeta = -$) valleys for ML MoS₂ in the presence of proximity-induced interactions.

The results shown in Figs. 2–5 indicate that in the presence of proximity-induced interactions such as Rashba SOC and exchange interaction, the electron energy degeneracy in K and K' valleys can be lifted and a nonzero in-plane electronic spin component can be achieved in ML MoS₂. Depending on the Fermi energy the system can be spin polarized. In Fig. 6, we show the Fermi energy as a function of total electron density n_e for $\lambda_R = 18.75$ meV (red curve) and $\lambda_R = 56.25$ meV (blue curve) for fixed $B_c = 10$ meV and $B_v = 5$ meV at $T = 4.2$ K. We also indicate which one of the four

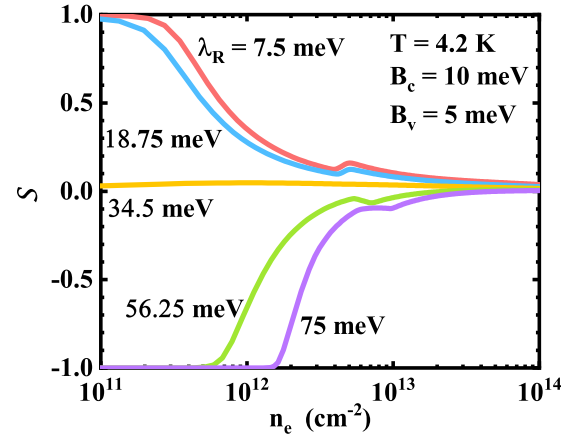


FIG. 8. The spin polarization \mathcal{S} as a function of total electron density for different Rashba parameters λ_R for fixed $B_c = 10$ meV and $B_v = 5$ meV. The results are obtained at $T = 4.2$ K.

spin-split conduction bands, $E_s^\zeta(0)$ with $\zeta = \pm$ and $s = \pm$, in blue/red arrows has the lowest energy. This is further illustrated in Fig. 7 where the occupation of the different bands in the two valleys are shown. With increasing n_e , the electron occupation of a single band to a situation where all four conduction bands in n-type ML MoS₂ are occupied can be achieved. In particular in Fig. 7, we present the electron occupation of the different split bands with different spin orientations at a relatively small Rashba parameter, just as the example for $\lambda_R = 18.75$ meV shown in Fig. 6. For a relatively large Rashba parameter, e.g., $\lambda_R = 56.25$ meV in Fig. 7, the electronic occupancy of the different bands are just exchanged for the two valleys but the spin states remain unchanged.

The spin polarization \mathcal{S} , defined by Eq. (8), as a function of total electron density n_e is shown in Fig. 8 for different Rashba parameters at $T = 4.2$ K. As shown in Fig. 3, when proximity-induced interactions are present in a n-type ML MoS₂, the split conduction bands with valley and spin index (ζ, s) are arranged from lower to higher energy as follows $(-, +), (+, -), (+, +),$ and $(-, -)$ for relatively small λ_R and as $(+, -), (-, +), (-, -),$ and $(+, +)$ for relatively large λ_R . Therefore, for small n_e only $(-, +)$ or $(+, -)$ states are occupied by electrons for relatively small or large λ_R [see Fig. 7(a)]. As a result, the electronic system is fully spin polarized. Because $(-, +)$ and $(+, -)$ states have opposite spin orientations, full polarization $\mathcal{S} = 1$ or $\mathcal{S} = -1$ can be achieved for relatively small or large λ_R . With increasing

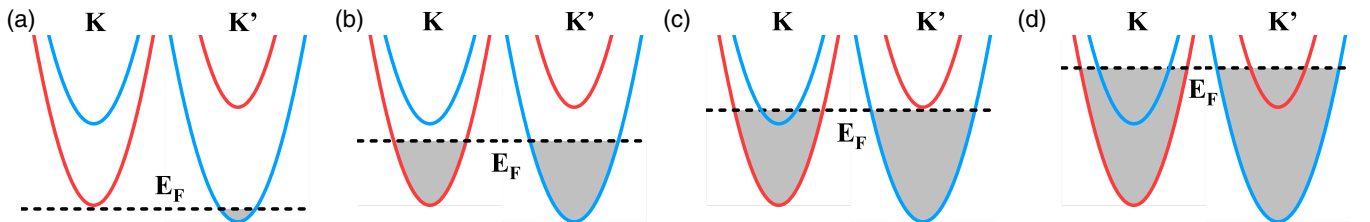


FIG. 7. Schematic presentation of the possible occupancy (shaded area) of electrons to different electronic states in the spin-split conduction band of K and K' valleys for a relatively small Rashba parameter. Here E_F is the Fermi energy which increases with total electron density n_e .

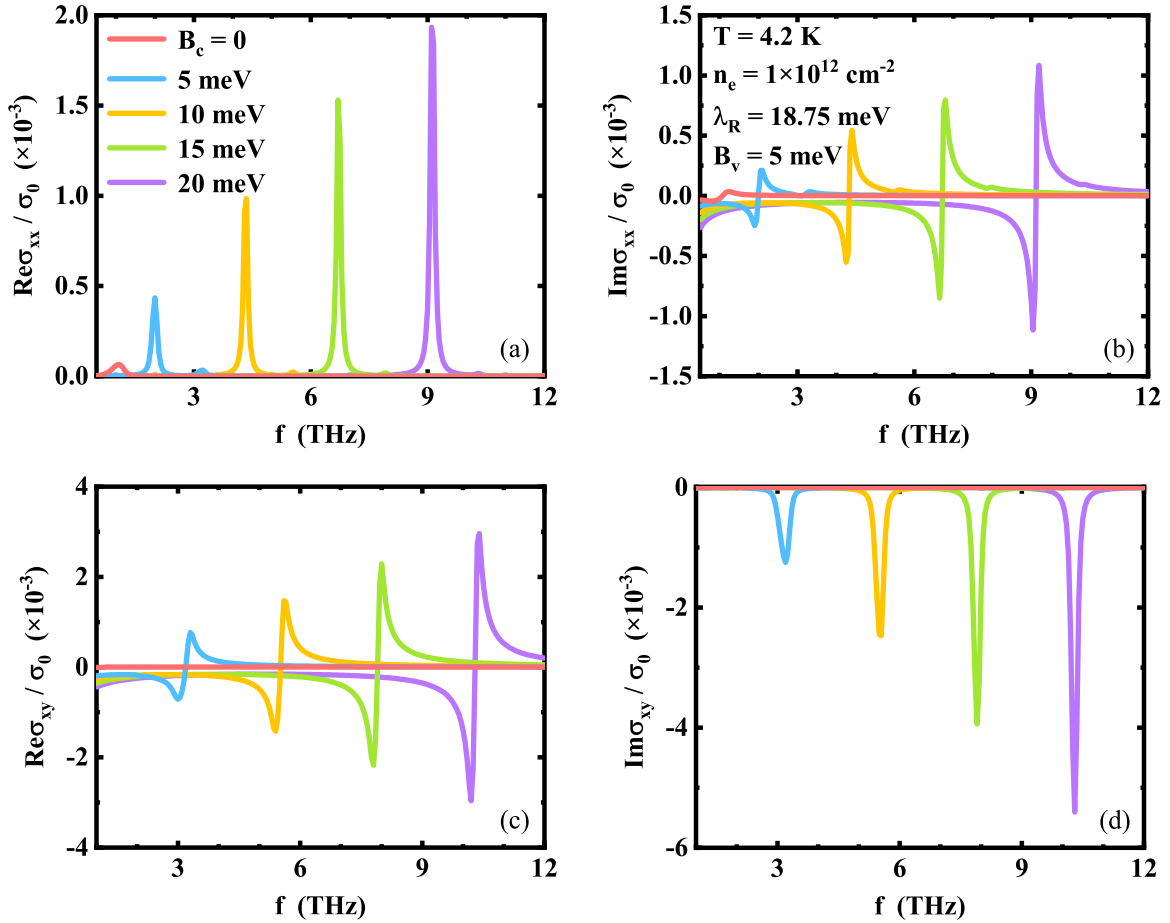


FIG. 9. The real and imaginary parts of the longitudinal σ_{xx} and transverse σ_{xy} optical conductivities as a function of radiation frequency $f = \omega/2\pi$ at fixed values of $\lambda_R = 18.75$ meV, $B_v = 5$ meV, $T = 4.2$ K, and $n_e = 1 \times 10^{12}$ cm $^{-2}$ for different Zeeman field factors B_c as indicated in the inset of (a). Here, $\sigma_0 = e^2/4\hbar$.

n_e , (+, -) or (-, +) states become occupied for relatively small or large λ_R [see Fig. 7(b)] so that $|\mathcal{S}|$ decreases with increasing n_e . With further increasing in n_e , (+, +) or (-, -) states become occupied for relatively small or large λ_R [see Fig. 7(c)] and, thus, a kinklike increase in $|\mathcal{S}|$ with n_e can be seen at about $n_e \sim 5 \times 10^{12}$ cm $^{-2}$. At relatively high electron densities, the highest (-, -) or (+, +) band is occupied for relatively small or large λ_R [see Fig. 7(d)] and $|\mathcal{S}|$ decreases with increasing n_e . When $n_e \gg 1$, $|\mathcal{S}| \rightarrow 0$. For the case of $\lambda_R = 34.5$ meV, because $E_-^+(k) \simeq E_+^-(k)$ and $E_+^+(k) \simeq E_-^-(k)$ (see Fig. 3), the electron occupation of the spin-split bands are roughly the same so that $|\mathcal{S}| \sim 0$ with varying n_e . The results shown in Fig. 8 demonstrate that the strength of the Rashba SOC plays a key role in affecting the spin polarization in ML MoS $_2$. When $B_c = 10$ meV and $B_v = 5$ meV, $\mathcal{S} > 0$ for $\lambda_R < 34.5$ meV, whereas $\mathcal{S} < 0$ for $\lambda_R > 34.5$ meV. The most important result shown in Fig. 8 is that at a fixed n_e , one can turn spin polarization from negative to positive by varying the strength of the Rashba SOC.

C. Optical conductivity

From Eqs. (11) and (12), we learn that the optical conductivity in n-type ML MoS $_2$ can be induced by intra- and interband electronic transitions within the split conduction

bands when the photon energy is less than the band gaps between conduction and valence bands. The intraband transition contributes only to a Drude-like longitudinal optical conductivity. Therefore, it is important to examine the longitudinal and transverse optical conductivities induced by interband or spin-flip transition within the conduction band in n-type ML MoS $_2$. Below, we present and discuss the numerical results for $\sigma_{xx} = \sigma_{xx,s}^+(\omega) + \sigma_{xx,s}^-(\omega)$ and $\sigma_{xy} = \sigma_{xy}^+(\omega) + \sigma_{xy}^-(\omega)$, whose expressions are given by Eqs. (11) and (12).

In Fig. 9, we show the real and imaginary parts of longitudinal σ_{xx} and transverse σ_{xy} optical conductivities induced by spin-flip transitions in a n-type ML MoS $_2$ as a function of radiation frequency $f = \omega/2\pi$ at a relatively small value of $\lambda_R = 18.75$ meV for fixed $B_v = 5$ meV, $T = 4.2$ K, and $n_e = 1 \times 10^{12}$ cm $^{-2}$ at different Zeeman field factors B_c . At $n_e = 1 \times 10^{12}$ cm $^{-2}$ and when $B_c = 0$ (the red curves), four conduction bands are all occupied by electrons. In this case, the lower energy (+, -) and (-, +) and higher energy (+, +) and (-, -) bands in K and K' valleys have roughly the same energies but with opposite signs of spin. As a result, $\sigma_{xy}^+(\omega) + \sigma_{xy}^-(\omega) \simeq 0$ so that the net Hall conductivity $\sigma_{xy} \rightarrow 0$. However, the longitudinal optical conductivity $\sigma_{xx} \neq 0$. These results are in line with those presented in Ref. [27]. When $B_c \geq 5$ meV, we find that only two lower energy bands (-, +) in K' valley and (+, -) in K valley are occupied

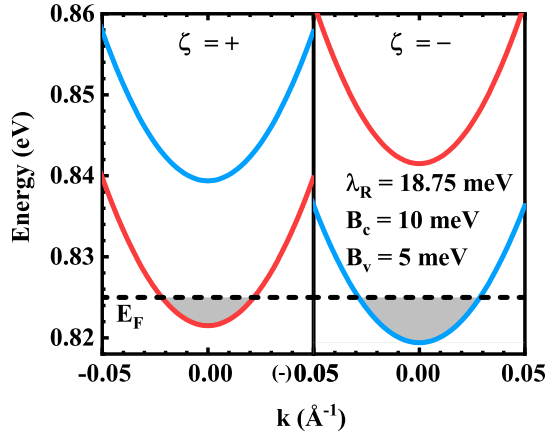


FIG. 10. The electron occupancy to split states in different valleys (shaded area) at the fixed values of $\lambda_R = 18.75$ meV, $B_c = 10$ meV, $B_v = 5$ meV, $T = 4.2$ K, and $n_e = 1 \times 10^{12}$ cm $^{-2}$.

with electrons. For example, at $B_c = 10$ meV the electron occupancy is shown in Fig. 10. In this case, because the energy degeneracy in the two valleys is lifted, $\sigma_{xy}^+(\omega)$ does not cancel out by $\sigma_{xy}^-(\omega)$ and, thus, both real and imaginary parts of $\sigma_{xy} \neq 0$ and the optical Hall effect can be observed. The peaks and valleys shown in σ_{xx} and σ_{xy} correspond to spin-flip transitions from lower occupied bands to higher empty bands accompanied by the absorption of photons. The peak positions corresponding to the resonance frequencies match well with the energy difference between spin-split conduction bands. For example, at $B_c = 10$ meV (see Fig. 10), the energy differences are about 17.88 meV and 22.1 meV for K and K' valley, respectively. As a result, the first absorption peak which comes from transitions in the K valley is at about 4.33 THz (the yellow curve in Fig. 9), and the second one is at about 5.35 THz. Interestingly, from Fig. 9 we see that the contribution to σ_{xx} comes mainly from $(+, -)$ to $(+, +)$ transition in K valley, whereas σ_{xy} mainly results from $(-, +)$ to $(-, -)$ transition in K' valley. Thus, only one peak can be obviously observed in σ_{xx} and σ_{xy} at a given $B_c \geq 5$ meV in Fig. 9. Two reasons are on the basis of this effect. Firstly, we note that for the case of $B_c \geq 5$ meV and a relatively small λ_R , the $(-, +)$ band in K' valley is lower than the $(+, -)$ band in K valley as shown in Fig. 10. Therefore, more electrons are populated in $(-, +)$ band in K' valley and $(-, +)$ to $(-, -)$ transition is the major channel for optical absorption. Secondly and more importantly, we find that the strength of the spin-flip transition in ML MoS $_2$ depends also on the selection rules given by Eq. (9c) and (9d), which is valley dependent as well. It can be proven that the modulus of $W_{\lambda'\lambda}^{xy}(\mathbf{k}, \mathbf{k}')$ in K' valley is larger than that in K valley, conversely the modulus of $W_{\lambda'\lambda}^{xx}(\mathbf{k}, \mathbf{k}')$ is larger in K valley than in K' valley. Such features do not change by varying the sample and material parameters. Consequently, one peak or valley can be obviously observed in σ_{xx} due mainly to the $(+, -)$ to $(+, +)$ transition in K valley and in σ_{xy} owing mainly to $(-, +)$ to $(-, -)$ transition in K' valley for fixed $B_c \geq 5$ meV in Fig. 9. Because electrons in the $(-, +)$ band have negative spin sign, $\text{Im}\sigma_{xy}$ is negative. We notice that another relatively small peak or valley induced by $(-, +)$ to

$(-, -)$ transition for σ_{xx} and induced by $(+, -)$ to $(+, +)$ transition for σ_{xy} can be numerically seen at respectively high and low frequency. Because the band splitting in K and K' valleys increases with B_c for fixed λ_R , one can observe blueshifts of the peaks or valleys in σ_{xx} and σ_{xy} .

In Fig. 11, we show the real and imaginary parts of longitudinal and transverse optical conductivities as a function of radiation frequency $f = \omega/2\pi$ at a relatively large $\lambda_R = 56.25$ meV for fixed values of $B_v = 5$ meV, $T = 4.2$ K, and $n_e = 1 \times 10^{12}$ cm $^{-2}$ for different Zeeman field factors B_c . For the case of $B_c = 0$, now only the lower $(+, -)$ and $(-, +)$ bands are occupied and the energies for these bands are roughly the same. Together with the higher $(+, +)$ and $(-, -)$ bands which have also roughly the same energies, the results for optical conductivity at $B_c = 0$ (red curves) are similar to those shown in Fig. 9. When $B_c \geq 5$ meV and $n_e = 1 \times 10^{12}$ cm $^{-2}$, we find that only two lower energy bands $(+, -)$ in K valley and $(-, +)$ in K' valley are occupied with electrons (see Fig. 12 for the case of $B_c = 10$ meV). In contrast to the case of small λ_R shown in Fig. 9, now the $(+, -)$ band in K valley is lower than the $(-, +)$ band in K' valley and the difference between $E_+^+(0) - E_+^-(0)$ and $E_-^-(0) - E_-^+(0)$, i.e., the energy difference between spin-split conduction bands, becomes significantly large. For $B_c = 10$ meV the values of $E_+^+(0) - E_+^-(0)$ and $E_-^-(0) - E_-^+(0)$ are about 24.88 meV and 14.97 meV, respectively, which also roughly match the resonance frequencies in σ_{xx} and σ_{xy} in Fig. 11 (see yellow curve). Therefore, more electrons are populated in K valley and $(+, -)$ to $(+, +)$ transition becomes the major channel for optical absorption. Together with the selection rule $W_{\lambda'\lambda}^{xx}(\mathbf{k}, \mathbf{k}')$ being favorable for spin-flip transition in K valley, an obvious optical absorption peak can be seen for σ_{xx} at a fixed B_c . Interestingly, although the selection rule $W_{\lambda'\lambda}^{xy}(\mathbf{k}, \mathbf{k}')$ is more favorable to spin-flip transitions in K' valley, we can still see contributions to σ_{xy} from both $(+, -)$ to $(+, +)$ and $(-, +)$ to $(-, -)$ transition events owing to the fact that there are more electrons in the K valley. Because $E_+^+(\mathbf{k}) - E_+^-(\mathbf{k})$ is markedly larger than $E_-^-(\mathbf{k}) - E_-^+(\mathbf{k})$ and $(+, -)$ states are occupied by much more electrons than $(-, +)$ (see Fig. 12), for $\text{Im}\sigma_{xy}$ we can observe a negative peak caused by $(-, +)$ to $(-, -)$ transition at a lower frequency and a positive peak induced by $(+, -)$ to $(+, +)$ transition at a higher frequency due to different spin orientations in the different valleys. Again, because $E_+^+(\mathbf{k}) - E_+^-(\mathbf{k})$ and $E_-^-(\mathbf{k}) - E_-^+(\mathbf{k})$ increase with B_c , blueshifts of the peak frequencies in $\text{Im}\sigma_{xy}$ can be achieved at a larger B_c . One of the most important results shown in Fig. 11 is that for a relatively large λ_R , we can obtain a negative $\text{Im}\sigma_{xy}$ at low frequency and a positive $\text{Im}\sigma_{xy}$ at high frequency.

In this study, we took the typical electron density as $n_e \sim 10^{12}$ cm $^{-2}$ when calculating numerically the optical conductivity in n-type ML MoS $_2$ while the doping level can be conveniently tuned through the application of a gate voltage [48]. We took relatively small values of $\lambda_R = 0.25\lambda_v = 18.75$ meV and $\lambda_R = 0.75\lambda_v = 56.25$ meV, $B_v = 5$ meV and $B_c \leq 20$ meV in our numerical calculations. It has been shown theoretically that B_c and B_v can be as large as 206 meV and 170 meV, respectively, when placing 2D TMD films on EuO substrate and λ_R can be as large as 72 meV [21]. Even so, we focused that it is still possible to observe the optical

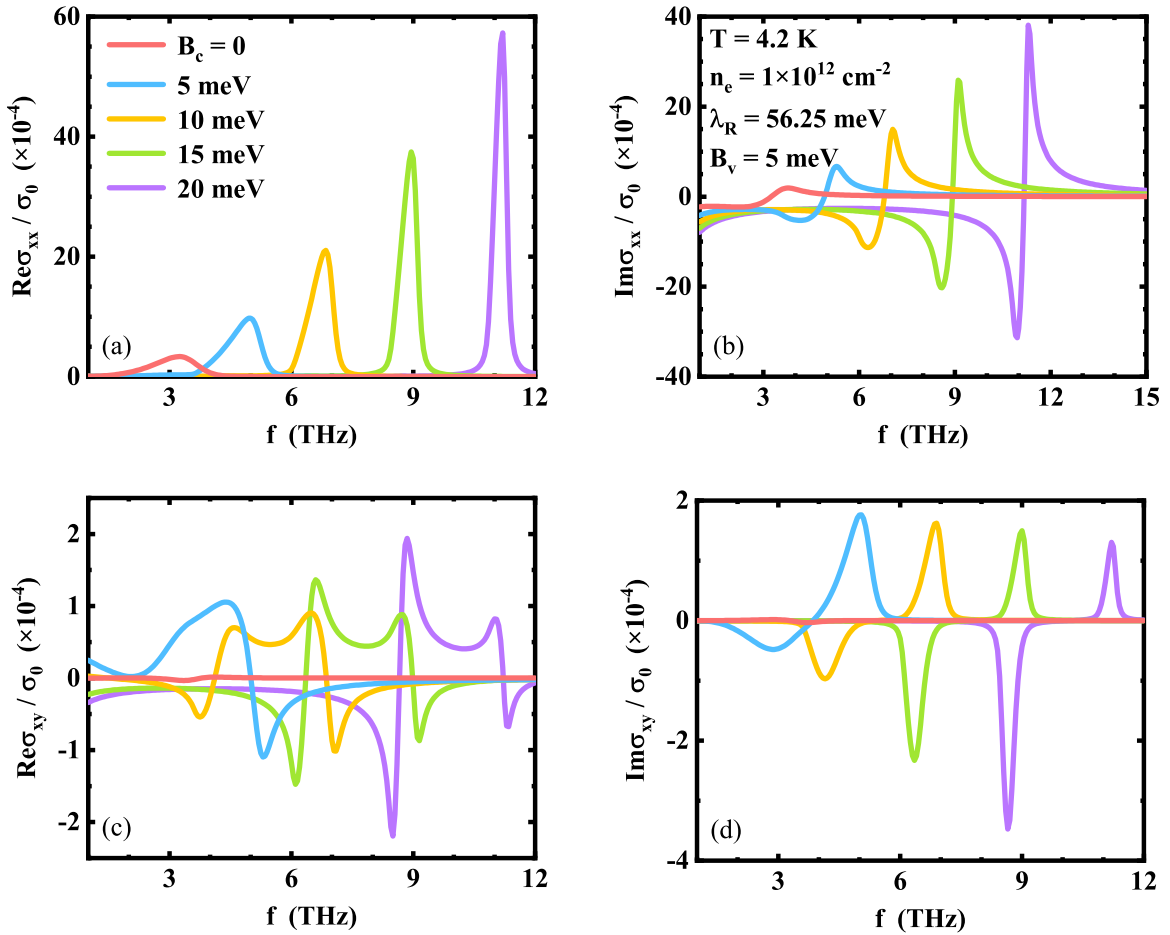


FIG. 11. The real and imaginary parts of the longitudinal and transverse optical conductivities as a function of radiation frequency $f = \omega/2\pi$ for fixed values of $\lambda_R = 56.25$ meV, $B_v = 5$ meV, $T = 4.2$ K, and $n_e = 1 \times 10^{12}$ cm $^{-2}$ for different Zeeman field B_c values. Here, $\sigma_0 = e^2/4\hbar$.

Hall effect in n-type ML MoS₂ in the THz regime. From the viewpoint of physics, the optical Hall effect corresponds to the Faraday optical rotation effect [49], where the Faraday rotation angle $\theta(\omega)$ and ellipticity $\eta(\omega)$ relate directly to the real and imaginary parts of the transverse optical conductivity

[50]. If $\theta(\omega)$ and $\eta(\omega)$ are nonzero, the sample device can turn a linearly polarized light field into an elliptically polarized one with a rotation angle. Experimentally, the Faraday rotation effect in a 2D electronic system can be observed by, e.g., THz TDS measurement [49]. Using this technique, a linearly polarized THz pulse field is applied to the sample and the polarization of the light beam transmitted through the sample is examined by a polarizer in the time domain. The amplitude and phase angle of the transmission signals in the frequency domain can be obtained after a Fourier transformation. Thus, via amplitude and phase angle of the transmission coefficient one can determine the Faraday rotation angle and ellipticity and, from them, determine the real and imaginary parts of $\sigma_{xy}(\omega)$. The results shown in Figs. 8 and 9 indicate that by using THz TDS, the optical Hall effect can be observed in n-type ML MoS₂ on, e.g., ferromagnetic substrates such as EuO or EuS which can lead to proximity-induced strong Rashba SOC and exchange interaction in ML MoS₂ [21,22].

The results presented and discussed in this paper indicate that the Rashba SOC plays an important role in affecting the electronic structure and in the observation of the optical Hall effect in ML MoS₂ based electronic systems. From, e.g., InGaAs/InAlAs based 2D spintronic systems, we know that the value of the Rashba parameter λ_R can be tuned efficiently by applying a gate voltage [51]. If we can apply a gate voltage

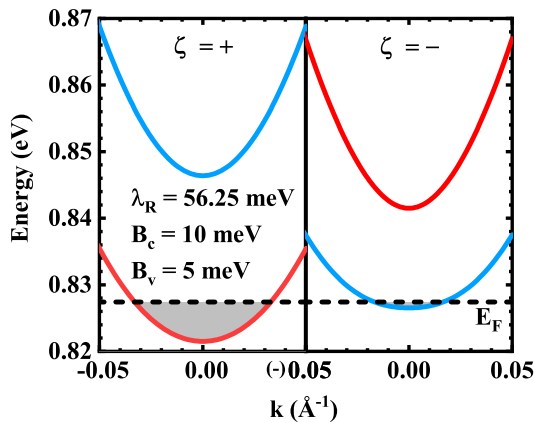


FIG. 12. The electron occupancy in different states and valleys (shaded area) at the fixed values of $\lambda_R = 56.25$ meV, $B_c = 10$ meV, $B_v = 5$ meV, $T = 4.2$ K, and $n_e = 1 \times 10^{12}$ cm $^{-2}$.

on, e.g., a ML MoS₂/EuO system and turn the value of λ_R , we can tune the sign of the spin polarization and of $\text{Im}\sigma_{xy}(\omega)$. Thus, such devices can be applied in, e.g., THz light polarizers and rotators.

IV. CONCLUSIONS

In this work, we have studied the electronic and optical properties of n-type ML MoS₂ in the presence of proximity-induced interactions such as Rashba SOC and exchange interaction. We have examined the roles of these interactions in affecting the band splitting in the different valleys, the in-plane spin orientation, the spin polarization, and the longitudinal and transverse optical conductivities of n-type ML MoS₂. The main conclusions obtained from this study are summarized as follows.

(1) In a 2D TMD material such as ML MoS₂, the Rashba SOC can result in an in-plane electronic spin and in the splitting of the conduction and valence bands in the different valleys. The presence of the proximity-induced exchange can further enhance the band splitting and break the symmetry of the electronic energy spectra in the two valleys, namely it can lift the energy degeneracy in K and K' valleys. Interestingly and importantly, it has been found from Fig. 3 that by varying the Rashba parameter we can tune the minimum of the conduction band in ML MoS₂ from spin-up states in K' valley to spin-down states in K valley.

(2) Due to the introduction of the in-plane spin and the lifting of the energy degeneracy in two valleys by proximity-induced interactions, spin polarization can be realized in n-type ML MoS₂. Similar to other electron gas systems, the spin polarization in n-type ML MoS₂ depends strongly on the electron density. We have demonstrated that at a fixed electron density, one can turn the sign of the spin polarization from negative to positive by varying the strength of the Rashba SOC.

(3) In the presence of proximity-induced interactions, due to the achievement of spin polarization in n-type ML MoS₂, the contributions to the transverse optical conductivity from electrons in K and K' valleys can no longer be canceled out. As a result, the net $\sigma_{xy}(\omega) = \sigma_{xy}^+(\omega) + \sigma_{xy}^-(\omega)$ becomes nonzero. This finding implies that the optical Hall effect can be observed in n-type ML MoS₂ by using linearly polarized THz light irradiation. Moreover, the sign of $\text{Im}\sigma_{xy}(\omega)$ can be tuned by varying λ_R and the peak frequency of $\text{Im}\sigma_{xy}(\omega)$ and $\text{Re}\sigma_{xx}(\omega)$ can be modulated by varying the Zeeman factor B_c .

(4) The selection rules for spin-flip optical transitions play an important role in the observation of the optical absorption and the optical Hall effect in ML MoS₂. We have found that for the conductivity $\sigma_{xx}(\omega)$ the selection rules are favored by electrons in K valley, while for $\sigma_{xy}(\omega)$ it is electrons in K' valley that mostly contribute.

At present, the valley Hall effect has been observed experimentally in 2D TMD based valleytronic systems by using circularly polarized radiation in infrared and visible bandwidth. In such a case, optical absorption is achieved via valence to conduction band transitions and photo-induced carriers and associated excitonic effect can be induced. Our results predict that the valley Hall or optical Hall effect can be observed in n-type ML MoS₂ via electronic transitions within the conduction band, by using linearly polarized THz field. The effects of photo-induced carriers and excitons can be neglected in this case. We hope that the important and interesting theoretically findings from this work can be verified experimentally in the near future.

ACKNOWLEDGMENTS

This work was supported by the National Natural Science Foundation of China (Grants No. U1930116, No. U1832153, and No. 11574319) and the Center of Science and Technology of Hefei Academy of Science (Grant No. 2016FXZY002).

-
- [1] D. Xiao, G. B. Liu, W. Feng, X. Xu, and W. Yao, *Phys. Rev. Lett.* **108**, 196802 (2012).
 - [2] T. Cao, G. Wang, W. Han, H. Ye, C. Zhu, J. Shi, Q. Niu, P. H. Tan, E. Wang, B. L. Liu, and J. Feng, *Nat. Commun.* **3**, 887 (2012).
 - [3] K. F. Mak, D. Xiao, and J. Shan, *Nat. Photonics* **12**, 451 (2018).
 - [4] J. R. Schaibley, H. Yu, G. Clark, P. Rivera, J. S. Ross, K. L. Seyler, W. Yao, and X. D. Xu, *Nat. Rev. Mater.* **1**, 16055 (2016).
 - [5] K. F. Mak and J. Shan, *Nat. Photonics* **10**, 216 (2016).
 - [6] O. Bleu, D. D. Solnyshkov, and G. Malpuech, *Phys. Rev. B* **95**, 235431 (2017).
 - [7] O. Bleu, D. D. Solnyshkov, and G. Malpuech, *Phys. Rev. B* **96**, 165432 (2017).
 - [8] H. Dery and Y. Song, *Phys. Rev. B* **92**, 125431 (2015).
 - [9] G. Wang, X. Marie, B. L. Liu, T. Amand, C. Robert, F. Cadiz, P. Renucci, and B. Urbaszek, *Phys. Rev. Lett.* **117**, 187401 (2016).
 - [10] G. B. Liu, W. Y. Shan, Y. Yao, W. Yao, and D. Xiao, *Phys. Rev. B* **88**, 085433 (2013).
 - [11] X. Xu, W. Yao, D. Xiao, and T. F. Heinz, *Nat. Phys.* **10**, 343 (2014).
 - [12] D. Xiao, W. Yao, and Q. Niu, *Phys. Rev. Lett.* **99**, 236809 (2007).
 - [13] D. Xiao, M. C. Chang, and Q. Niu, *Rev. Mod. Phys.* **82**, 1959 (2010).
 - [14] Y. D. Lensky, J. C. W. Song, P. Samutpraphoot, and L. S. Levitov, *Phys. Rev. Lett.* **114**, 256601 (2015).
 - [15] Y. K. Kato, R. C. Myers, A. C. Gossard, and D. D. Awschalom, *Science* **306**, 1910 (2004).
 - [16] K. F. Mak, K. L. McGill, J. Park, and P. L. McEuen, *Science* **344**, 1489 (2014).
 - [17] J. Lee, K. F. Mak, and J. Shan, *Nat. Nanotechnol.* **11**, 421 (2016).
 - [18] J. Lee, Z. Wang, H. Xie, K. F. Mak, and J. Shan, *Nat. Mater.* **16**, 887 (2017).
 - [19] G. Plechinger, T. Korn, and J. M. Lupton, *J. Phys. Chem. C* **121**, 6409 (2017).
 - [20] N. Ubrig, S. Jo, M. Philippi, D. Costanzo, H. Berger, A. B. Kuzmenko, and A. F. Morpurgo, *Nano. Lett.* **17**, 5719 (2017).
 - [21] J. Qi, X. Li, Q. Niu, and J. Feng, *Phys. Rev. B* **92**, 121403(R) (2015).

- [22] C. Zhao, T. Norden, P. Zhang, P. Zhao, Y. C. Cheng, F. Sun, J. P. Parry, P. Taheri, J. Q. Wang, Y. H. Yang, and T. Scrace, *Nat. Nanotechnol.* **12**, 757 (2017).
- [23] B. Yang, M. Lohmann, D. Barroso, I. Liao, Z. Lin, Y. Liu, L. Bartels, K. Watanabe, T. Taniguchi, and J. Shi, *Phys. Rev. B* **96**, 041409(R) (2017).
- [24] A. Soumyanarayanan, N. Reyren, A. Fert, and C. Panagopoulos, *Nature (London)* **539**, 509 (2016).
- [25] Q. F. Yao, J. Cai, W. Y. Tong, S. J. Gong, J. Q. Wang, X. Wan, C. G. Duan, and J. H. Chu, *Phys. Rev. B* **95**, 165401 (2017).
- [26] X. Liang, L. J. Deng, F. Huang, T. T. Tang, C. T. Wang, Y. P. Zhu, J. Qin, Y. Zhang, B. Peng, and L. Bi, *Nanoscale* **9**, 9502 (2017).
- [27] Y. M. Xiao, W. Xu, B. Van Duppen, and F. M. Peeters, *Phys. Rev. B* **94**, 155432 (2016).
- [28] I. Pupeza, R. Wilk, and M. Koch, *Opt. Express* **15**, 4335 (2007).
- [29] R. Ulbricht, E. Hendry, J. Shan, T. F. Heinz, and M. Bonn, *Rev. Mod. Phys.* **83**, 543 (2011).
- [30] J. Lloyd-Hughes and T. I. Jeon, *J. Infrared Millim. Terahertz Waves* **33**, 871 (2012).
- [31] C. Wang, W. Xu, H. Y. Mei, H. Qin, X. N. Zhao, C. Zhang, H. F. Yuan, J. Zhang, Y. Xu, P. Li, and M. Li, *Opt. Lett.* **44**, 4139 (2019).
- [32] Z. Y. Zhu, Y. C. Cheng, and U. Schwingenschlögl, *Phys. Rev. B* **84**, 153402 (2011).
- [33] H. Z. Lu, W. Yao, D. Xiao, and S. Q. Shen, *Phys. Rev. Lett.* **110**, 016806 (2013).
- [34] Z. Li and J. P. Carbotte, *Phys. Rev. B* **86**, 205425 (2012).
- [35] A. Kormányos, V. Zólyomi, N. D. Drummond, and G. Burkard, *Phys. Rev. X* **4**, 011034 (2014).
- [36] A. O. Slobodeniuk and D. M. Basko, *2D Mater.* **3**, 035009 (2016).
- [37] H. Min, J. E. Hill, N. A. Sinitsyn, B. R. Sahu, L. Kleinman, and A. H. MacDonald, *Phys. Rev. B* **74**, 165310 (2006).
- [38] S. V. Eremeev, I. A. Nechaev, Y. M. Koroteev, P. M. Echenique, and E. V. Chulkov, *Phys. Rev. Lett.* **108**, 246802 (2012).
- [39] D. Marchenko, A. Varykhalov, M. R. Scholz, G. Bihlmayer, E. I. Rashba, A. Rybkin, A. M. Shikin, and O. Rader, *Nat. Commun.* **3**, 1232 (2012).
- [40] P. D. C. King, R. C. Hatch, M. Bianchi, R. Ovsyannikov, C. Lupulescu, G. Landolt, B. Slomski, J. H. Dil, D. Guan, J. L. Mi, E. D. L. Rienks, J. Fink, A. Lindblad, S. Svensson, S. Bao, G. Balakrishnan, B. B. Iversen, J. Osterwalder, W. Eberhardt, F. Baumberger, and Ph. Hofmann, *Phys. Rev. Lett.* **107**, 096802 (2011).
- [41] S. Salehi and A. Saffarzadeh, *Surf. Sci.* **651**, 215 (2016).
- [42] Á. Bácsi and A. Virosztek, *Phys. Rev. B* **87**, 125425 (2013).
- [43] H. Shi, R. Yan, S. Bertolazzi, J. Brivio, B. Gao, A. Kis, D. Jena, H. G. Xing, and L. Huang, *ACS Nano* **7**, 1072 (2013).
- [44] E. J. Nicol and J. P. Carbotte, *Phys. Rev. B* **77**, 155409 (2008).
- [45] D. Svintsov, V. Ryzhii, A. Satou, T. Otsuji, and V. Vyurkov, *Opt. Express* **22**, 19873 (2014).
- [46] Y. Song and H. Dery, *Phys. Rev. Lett.* **111**, 026601 (2013).
- [47] H. Ochoa and R. Roldán, *Phys. Rev. B* **87**, 245421 (2013).
- [48] L. M. Yang, K. Majumdar, H. Liu, Y. C. Du, H. Wu, M. Hatzistergos, P. Y. Hung, R. Tieckelmann, W. Tsai, C. Hobbs, and P. D. Ye, *Nano. Lett.* **14**, 6275 (2014).
- [49] Y. Ikebe, T. Morimoto, R. Masutomi, T. Okamoto, H. Aoki, and R. Shimano, *Phys. Rev. Lett.* **104**, 256802 (2010).
- [50] R. F. O'Connell and G. Wallace, *Phys. Rev. B* **26**, 2231 (1982).
- [51] C. H. Yang, W. Xu, Z. Zeng, and C. S. Tang, *J. Phys: Condens. Matter* **18**, 6201 (2016).